

Stiffness and permeability multi-objective optimization of carbon-fiber-reinforced plastic mesostructures using homogenization method

Ryosuke Matsuzaki^{1,2} , Tomohiro Ishikawa¹,
Tomonaga Okabe^{3,4}, Yutaka Oya³ and Shigeki Yashiro⁵ 

Abstract

This paper presents a stiffness and permeability multi-objective optimization method for carbon-fiber-reinforced plastic mesostructures based on a homogenization method. To reduce the computational cost of dealing with multiple design variables for complicated fiber mesostructures, we generate and extract effective design variables from optimization results derived from a smaller number of design variables. We applied the proposed method to optimization of the in-plane and out-of-plane stiffness and permeability of non-crimp fabrics. The optimization results showed that the application of effective design variables enabled attainment of an improved elastic modulus and permeability. From investigations of the obtained optimized design, we clarified the trade-off relationship between the elastic modulus and permeability, and elucidated the effects of dimensions of non-crimp fabric mesostructures on the elastic modulus and permeability.

Keywords

Heterogeneous materials, homogenization, non-crimp fabric, permeability, porous media, shape optimization

Introduction

For fiber material used in the resin transfer molding (RTM) process of composites, optimization of the mesostructure is important for improving the productivity while maintaining a constant level of quality. Studies have been conducted on the elastic modulus and permeability coefficient of fiber material mesostructures using the homogenization method.^{1–4} However, to date, no studies have been conducted that successfully realized the optimization of multi-objective functions, such as those related to the elastic modulus and permeability coefficient for fiber material mesostructures.

Although the location in which design variables are set is an important factor for the optimization, the determination criteria remain unclear and are often dependent on the experience of the designers. Studies are therefore being conducted to achieve topology optimization^{5–9} that derives optimized shapes, even with no consideration of determination criteria. In topology optimization, there is no need to set design variables, and optimized shapes can be derived by setting only the boundary conditions. However, there are no reported

examples of the application of topology optimization to fiber material mesostructures with restrictive conditions for fabrication. This lack is attributed to the difficulty associated with obtaining optimization solutions.

Topology optimization is suitable for developing the fundamental design during the early stages of the process. Nevertheless, shape optimization is considered to have potential for implementation to practical design applications. As a result, to derive optimized solutions, many researchers have performed shape optimizations that incorporate several design variables that are

¹Department of Mechanical Engineering, Tokyo University of Science, Japan

²Institute of Fluid Science, Tohoku University, Japan

³Department of Aerospace Engineering, Tohoku University, Japan

⁴Department of Materials Science and Engineering, University of Washington, USA

⁵Department of Aeronautics and Astronautics, Kyushu University, Japan

Corresponding author:

Ryosuke Matsuzaki, Tokyo University of Science 2641 Yamazaki, Noda Chiba, 278-8510 Japan.

Email: rmatsuza@rs.tus.ac.jp

available in advance. To derive superior optimization solutions in an effective manner, design variables must be reduced to effective design variables.^{10–14} This is because the problematic aspect of increasing computational costs exists when the number of design variables is increased. However, there are two primary problems with previously used methods for optimization of fiber material mesostructures.

First, in the extraction of effective design variables, the optimization results were analyzed by incorporating as many design variables as possible into the optimization model. Because models that incorporate a large number of design variables have complex shapes, the mesh generation becomes a bottleneck during analyses owing to the amount of time required. Second, the criteria for the extraction of effective design variables are arbitrary and not based on any quantitative parameters.

In this paper, we therefore propose an optimization method for the stiffness and permeability of carbon-fiber-reinforced plastic (CFRP) mesostructures in an efficient manner. The method generates effective design variables from optimization results that are derived from a smaller number of design variables. Then, we examine the effectiveness of the proposed method by considering the optimization problems of the mesostructures of non-crimp fabric (NCF) material arranged in molding during the RTM process. Finally, we discuss the trade-off problems and dimension effects of multi-optimization of fiber material mesostructures.

Methods

Optimization outline

Figure 1 outlines the proposed method in comparison with a conventional method. The proposed method

involves the preparation of a simple fiber-material mesostructure model that is expressed using the minimum number of design variables to minimize the computational time. We employ the homogenization method to derive the elastic modulus and permeability coefficient of the fiber material mesostructure. To maximize the elastic and permeability coefficients, we optimize the dimensions of the fiber-material mesostructure using the non-dominated sorting genetic algorithm 2 (NSGA-2),¹⁵ which is a multi-objective genetic algorithm (MOGA).

The optimization results are next used as sample data. These data include new design variables, which are dependent variables of the original design variables. The latter variables were produced by dividing the optimization model into regions. Here, we verify the multicollinearity using a scatter plot matrix (SPM), while variables that have a high correlation coefficient are combined. After that, we generate the mathematical formula for predicting the value of the objective functions. To this end, we use genetic programming (GP) to clarify the relationship between the design variables and the objective functions, as well as to generate and extract effective design variables for improving the optimization solutions. The mathematical formula we use to predict the value of the objective functions is referred to as the prediction model, as described below.

To determine the relationship between the design variables and the objective functions, an evaluation standard for the prediction model must be established when deriving a prediction model using the GP. We use the GP to incorporate the concept of Akaike's information criterion (AIC)¹⁶ and the tolerance (TOL)¹⁷ concept into the evaluation standard for deriving prediction models. The AIC indicates a good fit to the sample data and prevents overfitting through

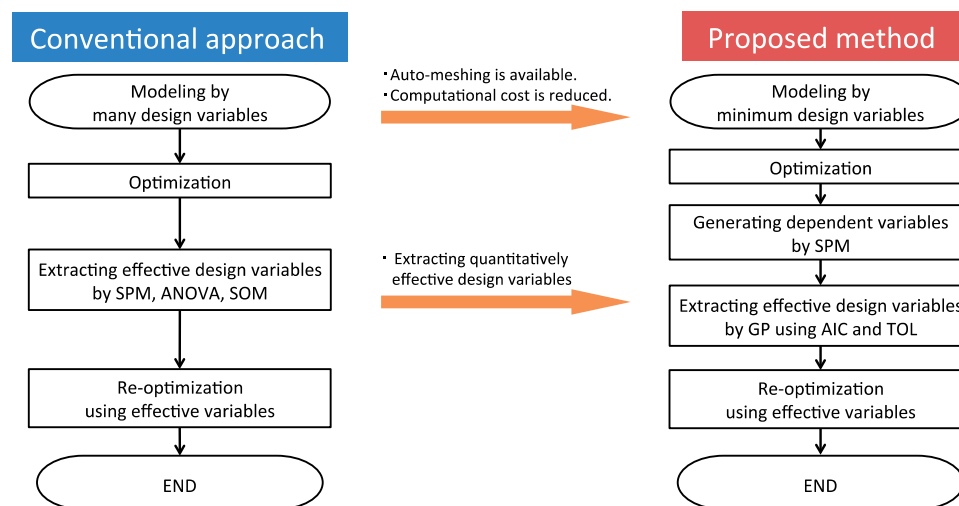


Figure 1. Conceptual scheme of the multi-objective optimization of fiber-reinforced composites using the homogenization method.

minimization. Furthermore, we can use the TOL to express the relationship between the design variables and the objective functions with a valid prediction model because multi-collinearity, which renders as uncertain the codes that are included in the prediction model, is prevented. Terms that are included in the prediction model having large-valued coefficients may be extracted as effective design variables.

Calculation of elastic and permeability coefficient for the fiber-material mesostructure

In the case of fiber-reinforced composites, Young’s modulus and the shear modulus can be predicted using Halpin–Tsai equations,¹⁸ while the permeability coefficient can be predicted using the Gebart method.¹⁹ However, these methods cannot predict the macroscopic properties of CFRP fabrics that have arbitrary mesoscale structures. The homogenization method²⁰ must therefore be used to connect macro- and mesoscales.

The homogenization method defines the macrostructure (region Ω) having the same size as the inhomogeneous overall structure of the target considered for the analysis, as well as the periodical unit structure that has micro-inhomogeneity, as the mesostructure (region Y). The ratio of the representative length of the macrostructure l_Ω to the representative length of mesostructure l_Y is also defined, as shown in equation (1) (see Figure 2).

$$\lambda = \frac{l_Y}{l_\Omega} \tag{1}$$

Furthermore, the coordinate of the macrostructure is defined by \mathbf{x} , while the coordinate of the mesostructure is defined by \mathbf{y} . The relationship between \mathbf{x} and \mathbf{y} is described below using scale ratio λ

$$\mathbf{y} = \frac{\mathbf{x}}{\lambda} \tag{2}$$

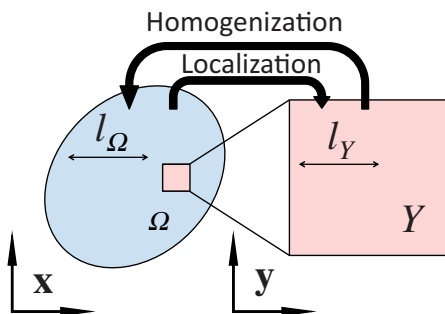


Figure 2. Multiscale simulation of the elastic body using the homogenization method.

The following equilibrium equation, strain–displacement expression, and constitutive equation derived from the mechanics of elasticity are used to derive the elastic modulus of the macrostructure elicited by the mesostructure

$$\frac{\partial \sigma_{ij}^\lambda}{\partial x_i} = 0 \tag{3}$$

$$\varepsilon_{kl}^\lambda = \frac{1}{2} \left(\frac{\partial u_k^\lambda}{\partial x_j} + \frac{\partial u_j^\lambda}{\partial x_i} \right) \tag{4}$$

$$\sigma_{ij}^\lambda = D_{ijkl}^\lambda \varepsilon_{kl}^\lambda \tag{5}$$

where the physical quantities of the overall structure depend on the mesostructure. Accordingly, the superscript λ is added. Furthermore, u_i^λ is the displacement of the overall structure. The principle of virtual work for the overall structure shown below is derived by applying to equation (3) the boundary conditions for the overall structure as well as the Gauss divergence theorem

$$\int_{\Omega^\lambda} \sigma_{ij}^\lambda \frac{\partial \delta u_i^\lambda}{\partial x_j} d\Omega = \int_{\Gamma_i^\lambda} t_i \delta u_i^\lambda d\Gamma \tag{6}$$

where Γ_i^λ is the mechanical boundary surface for the overall structure, while t_i is the surface force per unit area.

Let us consider that the displacement u_i^λ for the overall structure, which depends on the mesostructure, can be expressed using an asymptotic expression, as shown by the following equation

$$\begin{aligned} u_i^\lambda &= u_i^0(\mathbf{x}) + \lambda u_i^1(\mathbf{x}, \mathbf{y}) + \lambda^2 u_i^2(\mathbf{x}, \mathbf{y}) + \dots \\ &\cong u_i^0(\mathbf{x}) + \lambda u_i^1(\mathbf{x}, \mathbf{y}) \end{aligned} \tag{7}$$

where u_i^0 is the displacement of the macrostructure and $u_i^1(\mathbf{x}, \mathbf{y})$ is the displacement disturbance of the mesostructure. Equation (7) expresses the displacement of the overall structure, together with the mesostructure displacement disturbance and macrostructure displacement. The mesostructure unit is assumed to be repeated infinitely using the homogenization method. In other words, we assign the extreme boundary of $\lambda \rightarrow 0$. The partial differential of the overall structure then becomes equation (8), as shown below, by using the combination of equations (2) and (7)

$$\frac{\partial u_i^\lambda}{\partial x_j} = \frac{\partial u_i^0}{\partial x_j} + \frac{\partial u_i^1}{\partial y_j} \tag{8}$$

We apply the averaging approximation theorem expressed by equation (9) to separate the principle of

virtual work for the overall structure, as expressed by equation (6), into the integration domains of the macrostructure and mesostructure

$$\lim_{\lambda \rightarrow 0} \int_{\Omega^\lambda} \psi^\lambda d\Omega = \int_{\Omega} \frac{1}{|Y|} \int_Y \psi(\mathbf{x}, \mathbf{y}) dY d\Omega \quad (9)$$

The integrand $\psi(\mathbf{x}, \mathbf{y})$ represents an inhomogeneous physical quantity and a material constant. For equation (9) to be valid, a periodicity must exist for Y .

We substitute equations (3), (5), (7), and (8) into equation (6), and we apply the averaging approximation theorem to derive the macrostructural formula of equation (10) and the mesostructural formula of equation (11).

$$\int_{\Omega} \frac{1}{|Y|} \int_Y D_{ijkl} \left(\frac{\partial u_k^0}{\partial x_l} + \frac{\partial u_l^1}{\partial y_l} \right) \frac{\partial \delta u_i^0}{\partial x_j} dY d\Omega = \int_{\Gamma} t_i \delta u_i^0 d\Gamma \quad (10)$$

$$\frac{1}{|Y|} \int_Y D_{ijkl} \left(\frac{\partial u_k^0}{\partial x_l} + \frac{\partial u_l^1}{\partial y_l} \right) \frac{\partial \delta u_i^1}{\partial y_j} dY = 0 \quad (11)$$

We discretize equations (10) and (11) using the finite-element method (FEM) based on the hypothesis that the mesostructural displacement disturbance u_i^1 is proportional to the macrostructural strain, represented by equation (12), to derive the homogenized macrostructural elastic stiffness constant of equation (13)

$$u_i^1(\mathbf{x}, \mathbf{y}) = \chi_i^{kl}(\mathbf{x}, \mathbf{y}) \frac{\partial u_k^0}{\partial x_l} \quad (12)$$

$$D_{ijmn}^H = \frac{1}{|Y|} \int_Y (D_{ijmn} - D_{ijkl} B_{l\alpha}^1 \chi_{k\alpha}^{mn}) dY \quad (13)$$

where superscript H signifies the homogenized macrostructural model. $\chi_i^{kl}(\mathbf{x}, \mathbf{y})$ is referred to as the characteristic displacement function, with periodicity in Y . Subscript α in equation (13) represents the constituent node number of an element.

Similar to the derivation of the elastic modulus, we consider the Stokes flow of Newtonian fluid, and we consider the solid phase to be undeformed to simplify the derivation of the permeability coefficient. There are two governing equations, namely the equation of continuity and the balance equilibrium of the liquid phase, and we use the following equations

$$\frac{\partial v_i^\lambda}{\partial x_i} = 0 \quad (14)$$

$$-\frac{\partial p^\lambda}{\partial x_i} + \mu^\lambda \frac{\partial^2 v_i^\lambda}{\partial x_j \partial x_j} = 0 \quad (15)$$

where p represents the pressure, v_i denotes the flow velocity, and μ represents the viscosity. Because the physical quantities for the overall structure depend on the mesostructure, we add superscript λ . The boundary condition for the solid and liquid boundaries is the nonslip condition

$$v_i^\lambda = 0 \quad \text{on } \Gamma \quad (16)$$

Here, when the extreme boundary of $\lambda \rightarrow 0$ is assigned, μ^λ is defined as

$$\mu^\lambda = \lambda^2 \mu \quad (17)$$

The above assumes that, when the extreme boundary of $\lambda \rightarrow 0$ is assigned, the overall flow of the liquid becomes slower with respect to λ^2 . Let us consider that the flow velocity and pressure for the overall structure can be expressed using an asymptotic expression, as was the case in the previous section

$$v_i^\lambda(\mathbf{x}, \mathbf{y}) = v_i^0(\mathbf{x}, \mathbf{y}) + \lambda v_i^1(\mathbf{x}, \mathbf{y}) + \lambda^2 v_i^2(\mathbf{x}, \mathbf{y}) + \dots \cong v_i^0(\mathbf{x}, \mathbf{y}) + \lambda v_i^1(\mathbf{x}, \mathbf{y}) \quad (18)$$

$$p^\lambda(\mathbf{x}, \mathbf{y}) = p^0(\mathbf{x}, \mathbf{y}) + \lambda p^1(\mathbf{x}, \mathbf{y}) + \lambda^2 p^2(\mathbf{x}, \mathbf{y}) + \dots \cong p^0(\mathbf{x}, \mathbf{y}) + \lambda p^1(\mathbf{x}, \mathbf{y}) \quad (19)$$

where v_i^j and p^j are periodic in Y . Based on the relationship in equation (2), we can express the chain rule of differentiation as follows

$$\frac{\partial}{\partial x_i} \Big|_{\Omega^\lambda} = \frac{1}{\lambda} \frac{\partial}{\partial y_i} \Big|_{Y_f} + \frac{\partial}{\partial x_i} \Big|_{\Omega_f} \quad (20)$$

Equations (14) and (15) must be valid for the respective orders of λ . Equations (18) and (20) are therefore substituted into equation (14) and rearranged for the respective orders of λ .

$$\frac{\partial v_i^0}{\partial y_i} = 0 \quad (\text{order of } \lambda^{-1}) \quad (21)$$

$$\frac{\partial v_i^0}{\partial x_i} + \frac{\partial v_i^1}{\partial y_i} = 0 \quad (\text{order of } \lambda^0) \quad (22)$$

Rearranging equation (15) in a similar manner results in the following

$$-\frac{\partial p^0}{\partial y_i} = 0 \quad (\text{order of } \lambda^{-1}) \quad (23)$$

$$-\frac{\partial p^1}{\partial y_i} - \frac{\partial p^0}{\partial x_i} + \mu \frac{\partial}{\partial y_j} \frac{\partial v_i^0}{\partial y_j} = 0 \quad (\text{order of } \lambda^0) \quad (24)$$

The following equation must be valid in order for equation (22) to have v^1 as the solution on the mesoscale:

$$\int_Y \frac{\partial v_i^0}{\partial x_i} dy = 0 \tag{25}$$

V_i is the flow velocity on the macroscale and is defined as

$$V_i = \frac{1}{Y} \int_Y v_i^0 dy \tag{26}$$

Based on equations (25) and (26), it then becomes evident that the equation of continuity on the macroscale must be valid, as shown by the following equation

$$\frac{\partial V_i}{\partial x_i} = 0 \tag{27}$$

From equation (23), we see that p^0 is not a function of y .

Let us assume that the hypothesis in equations (28) and (29) is valid based on the use of the characteristic function^{21–23}

$$v_i^0 = -\frac{\kappa_i^j \partial p^0}{\mu \partial x_j} \tag{28}$$

$$p^1 = -A_j \frac{\partial p^0}{\partial x_j} + \bar{p}^1(x_j) \tag{29}$$

where κ_i^j and A_j are characteristic functions with periodicity in Y . In the same way, p denoted with a bar is independent of y_j . If we substitute equation (28) into equation (21), and equations (28) and (29) are substituted into equation (24), we can derive the following^{3,21,22,24,25}

$$\frac{\partial \kappa_i^j}{\partial y_i} = 0 \tag{30}$$

$$-\frac{\partial A_j}{\partial y_i} + \frac{\partial}{\partial y_k} \frac{\partial \kappa_i^j}{\partial y_k} = -\delta_{ij} \tag{31}$$

Similarly, for the boundary conditions, we substitute equation (28) into equation (16) to derive the following

$$\kappa_i^j = 0 \quad \text{on } \Gamma \tag{32}$$

Equations (30) to (32) comprise the governing equations on the mesoscale. By discretizing equations (30) and (31) using the FEM and GLS method,²⁶ we can derive κ_i^j (see Appendices 1 and 2). The homogeneous

permeability coefficient tensor K_{ij} is derived by taking the volume average of κ_i^j in unit cells, as described below

$$K_{ij} = \frac{1}{Y} \int_Y \kappa_i^j dY \tag{33}$$

The validation of the homogenized permeability calculation is described in Appendix 2.

Genetic programming for the prediction model

For a good fit of the homogeneous elastic modulus and the permeability coefficient, we use the GP to optimize the prediction model, which indicates the relationship between the objective functions and design variables with the added dependent variables. We derive the dependent variables by dividing the model into regions and expressing the regions with combinations of design variables. Furthermore, we normalize the respective variables using equation (34) to assign a value within the range of zero to one. This is because we compare the impact of the design variables in terms of the coefficients when the effective design variables are extracted from the prediction model

$$\tilde{x}_i = \frac{(x_i - x_{\min})}{(x_{\max} - x_{\min})} \tag{34}$$

In the above equation, the variable denoted with a tilde (\sim) represents a normalized variable.

When deriving a prediction model using the GP, we implement the AIC to a degree of fitness f_i . We establish the AIC using the unbiased estimator of the expected average logarithmic likelihood with reference to the Kullback–Liebler (K-L) divergence, which indicates the quality of the prediction model. The AIC for the multiple regression models is described below because prediction models derived by the GP are multiple regression models

$$f_i = n \left(\ln \left(2\pi \frac{S_e}{n} \right) + 1 \right) + 2(m + 2) \tag{35}$$

where n represents the number of samples, S_e denotes the sum-of-squares error, and m represents the number of explanatory variables. The first term on the right side of equation (35) signifies the size of the error for the prediction model and the target of prediction, while the second term signifies the complexity of the equation for the prediction model. We can derive the intended prediction model by minimizing f_i .

Furthermore, there exists a problem of multi-collinearity upon generating a prediction model. Multi-collinearity is a problem that occurs when a

number of variables with a high degree of correlation exist within a prediction model. The task performed involves the visualization of the correlation coefficient between variables, which include newly defined dependent variables. This is achieved using the SPM shown in Figure 3 as well as classifying those variables that have a correlation coefficient exceeding 0.7 as the same variables, thereby reducing them into one.

To prevent multi-collinearity of terms in the prediction models generated with the GP, we use the TOL, which is one of the indices for determining multi-collinearity. The equation used to derive the TOL is shown below.

$$TOL_i = 1 - R_i^2 \tag{36}$$

In equation (36), R_i represents the determination coefficient, with the number of degrees-of-freedom being adjusted when the regression model is set up in

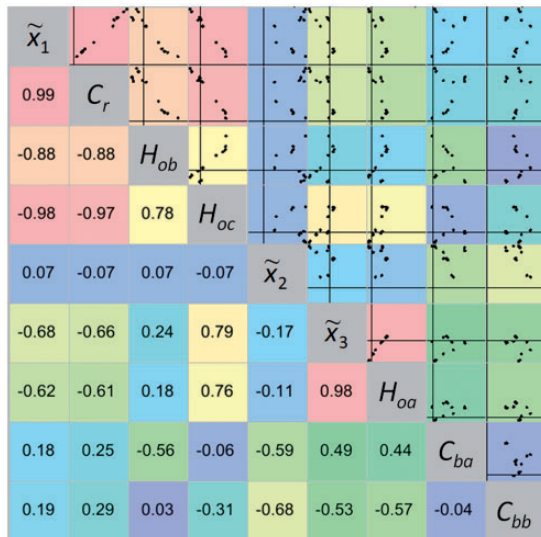


Figure 3. Scatter plot matrix showing the value of the correlation coefficient.

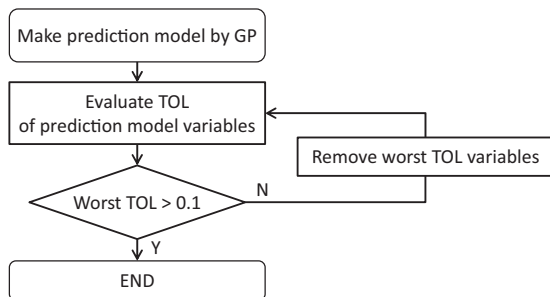


Figure 4. Scheme used to eliminate the multi-correlation in the prediction model.

accordance with variable i . As described in Figure 4, to prevent multicollinearity, we derive a prediction model with a TOL for all variables equal to 0.1 or higher by repeating the TOL evaluation of all variables and removing the worst TOL variables. In this manner, we derive the variables that significantly affect the objective functions, and they are used as references for the design variables for re-optimization.

Application to non-crimp fabric

Modeling

We applied to NCF the extraction method of the effective design variables proposed in this paper. We fabricated an NCF model with a mesostructure, as shown in Figure 5, and performed a multi-objective optimization using NSGA-2. The fiber bundle is modeled by orthotropic elastic materials, whereas the resin is an isotropic elastic material. The properties of these materials are listed in Table 1. The objective functions consisted of the four coefficients, namely the elastic modulus and permeability coefficient in the in-plane and out-of-plane directions. The four objective functions are optimized

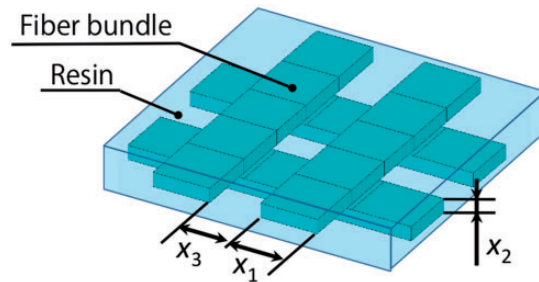


Figure 5. Design variables of the unit cell of the non-crimp fabric operating at multi-objective genetic algorithm (MOGA0).

Table 1. Material properties of fiber bundle and resin.

Fiber bundle ^a (V_f 70%)	Young's modulus	E_1 (GPa)	176
		E_2, E_3 (GPa)	32.8
	Shear modulus	G_{12}, G_{13} (GPa)	8.55
		G_{23} (GPa)	5.46
	Poisson's ratio	ν_{12}, ν_{13}	0.24
ν_{23}		0.19	
Resin	Density	ρ (g/cm ³)	1.6
	Young's modulus	E (GPa)	3.50
	Poisson's ratio	ν	0.37
	Density	ρ (g/cm ³)	1.0

^aSubscript 1 denotes the fiber bundle direction, whereas subscripts 2 and 3 denote the transverse direction.

simultaneously by obtaining the Pareto front, which is the non-inferior solution group. Note that the Pareto front cannot be obtained by the single objective function comprising all parameters with some weights. There were three design variables, as shown in Figure 5, namely the fiber-bundling width (x_1), fiber-bundle thickness (x_2), and fiber-bundle interval in the cross-direction within a unit cell (x_3). The unit cell repeats periodically in three directions in this study. It should be noted that directions 1 and 2 (i.e. in-plane) are equivalent for the unit cell.

Generation and extraction of effective design variables

The NCF model used in this study classifies the regions of resins from the upper surface, as shown in Figure 6. We then newly define the proportion of the volume of resin in each region with respect to the volume of the unit cell as dependent variables, C_r , C_{ba} , C_{bb} , H_{oa} , H_{ob} , and H_{oc} .

To reduce the sum of the original design variables normalized by the length of the unit cell, \tilde{x}_1 , \tilde{x}_2 , and \tilde{x}_3 , and the six above-mentioned newly defined dependent variables, we obtain their correlation coefficients using the SPM. Based on the results, x_1 , C_r , H_{ob} , and H_{oc} are closely correlated and reduced to x_1 . Meanwhile, x_3 and H_{oa} are reduced to x_3 , which results in the formulation of a prediction model with five variables, namely x_1' , x_2' , x_3' , C_{ba} , and C_{bb} .

We employ the cross-validation method to verify the quality of the fit for the prediction model.²⁷ This is performed by separating all the data into the training data used for the generation of the prediction model and the test data that are handled as true values. The leave-one-out cross validation involves the use of respective models included in the Pareto solution as test data in sequence.

The results obtained from conducting a leave-one-out cross validation on respective objective functions

are shown in Figure 7. The relationship between the estimated values and true values indicates that the determination coefficient is equal to one in Figure 7(a) and (b), while it is 0.94 in Figure 7(c) and (d). In both cases, the values exceed 0.9, and the model is therefore considered a good-quality prediction model. We derive the following equations after performing the GP.

$$E_1 = 7.0 \times 10^3 \times \tilde{x}_1 - 8.6 \times 10^2 \times \tilde{C}_{bb} - 4.8 \times 10^2 \times \tilde{C}_{ba} + 4.0 \times 10^2 \times \tilde{x}_2 \times (\tilde{x}_1 + \tilde{C}_{bb}) + 1.8 \times 10^2 \times \tilde{x}_2^3 \times \tilde{C}_{ba} + 1.0 \times 10^4 \quad (37)$$

$$E_3 = 2.5 \times 10^3 \times \tilde{x}_1 - 1.7 \times 10^3 \times (\tilde{x}_1^2 \times \tilde{x}_3 \times \tilde{C}_{bb}^2) + 3.8 \times 10^2 \times \tilde{x}_2 + 2.8 \times 10^1 \times \tilde{x}_2^2 \times (\tilde{x}_1 + \tilde{x}_3) + 5.6 \times 10^3 \quad (38)$$

$$K_1 = -2.1 \times 10^{-3} \times (\tilde{x}_1) + 2.7 \times 10^{-3} \quad (39)$$

$$K_3 = -9.4 \times 10^{-3} \times (\tilde{x}_1) + 9.6 \times 10^{-3} \quad (40)$$

Equations (37) to (40) are the prediction equations for the in-plane and out-of-plane elastic modulus and permeability coefficients. An overall assessment of equations (37) to (40) reveals that \tilde{x}_1 is included in all of the prediction models, and the coefficients are larger, significantly affecting the objective functions. A careful assessment of \tilde{x}_1 also reveals that the relationship between the elastic modulus and permeability coefficients is a trade-off relationship.

Because x_1 is a variable that is highly correlated with C_r , H_{ob} , and H_{oc} , we derive a design knowledge indicating that, in addition to the existing design variables, increasing the design variables with respect to the

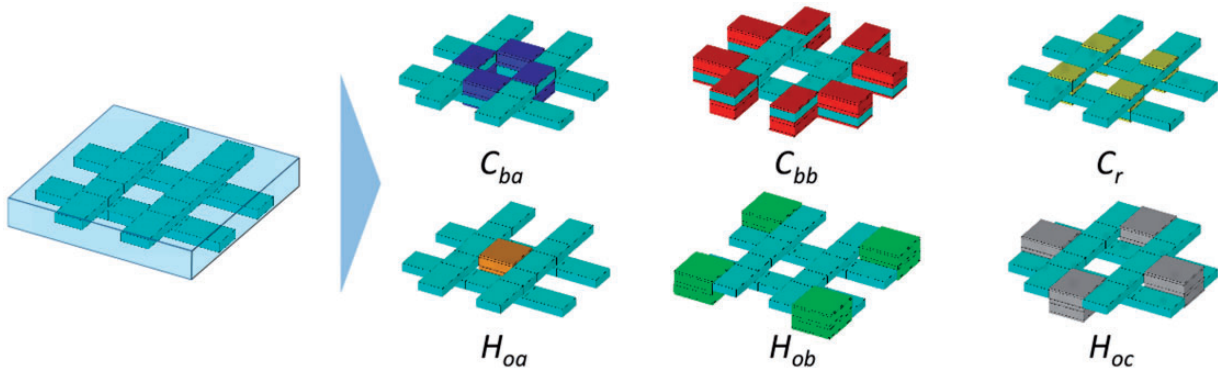


Figure 6. Defined dependent variables obtained by dividing the optimization model into regions.

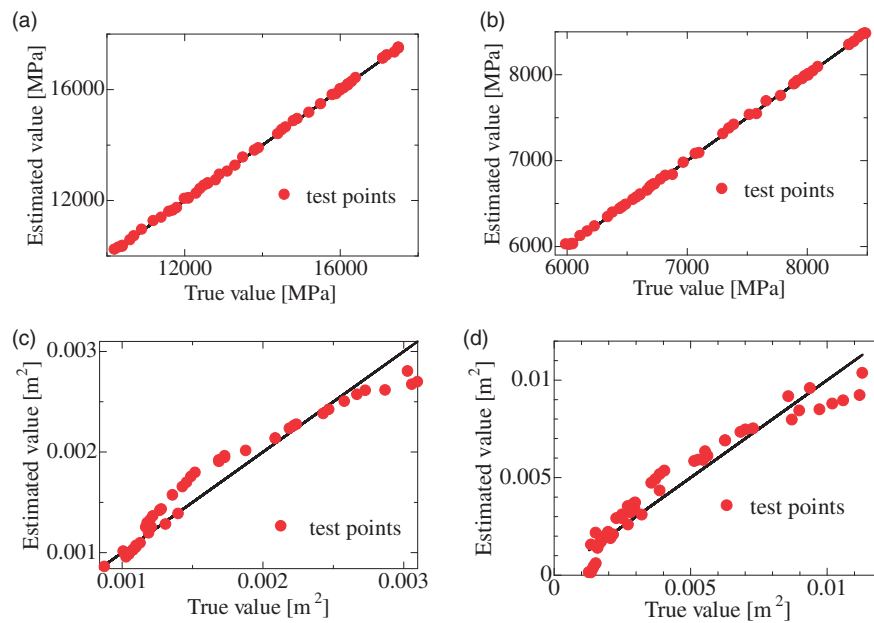


Figure 7. Validation of the genetic programming (GP) prediction model derived using the proposed method. (a) In-plane Young's modulus, (b) Out-of-plane Young's modulus, (c) In-plane permeability and (d) Out-of-plane permeability.

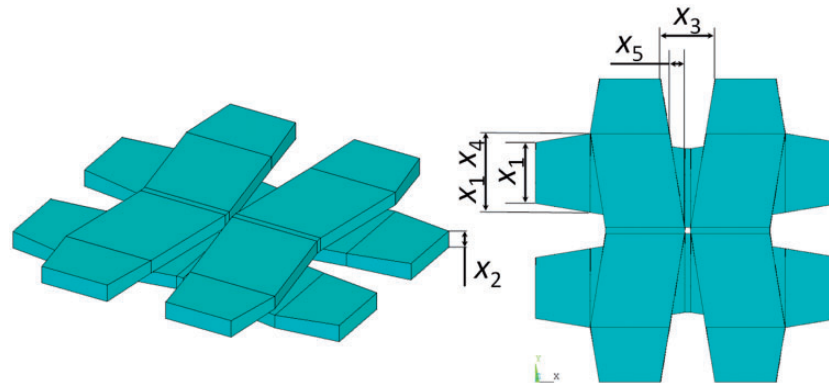


Figure 8. Design variables of the unit cell of the non-crimp fabric applied to the effective design variables operating at the multi-objective genetic algorithm (MOGA).

regions of C_r , H_{ob} , and H_{oc} may realize an improved fiber material mesostructure.

Re-optimization

Reflecting the design knowledge of the NCF model derived in the preceding section, we increase the number of design variables in the regions C_r , H_{ob} , and H_{oc} , as the fiber-bundle width (x_1), fiber-bundle thickness (x_2), fiber-bundle width interval (x_3), change rate of the fiber-bundle width (x_4), and fiber-bundle offset (x_5), as shown in Figure 8. It should be noted that the fiber-bundle width change rate and fiber-bundle offset can be controlled by stitching fiber bundles together²⁸ in actual applications. The cross-sectional areas of the fiber bundles and fiber-volume fraction of the fiber bundle are

assumed to be fixed. Note that the fiber volume fraction in the unit cell is not constant.

Figure 9 shows the Pareto solutions of in-plane and out-of-plane properties obtained by optimization before and after application of the effective design variables. The area marked by the dashed line indicates that the Pareto solutions improve upon the application of effective design variables. From Figure 9, we confirm that the solutions of stiffness and permeability multi-objective optimization improve in the overall Pareto front by applying effective design variables.

Discussion

The optimal shapes that maximize each objective function are shown in Figure 10. The maximum values for

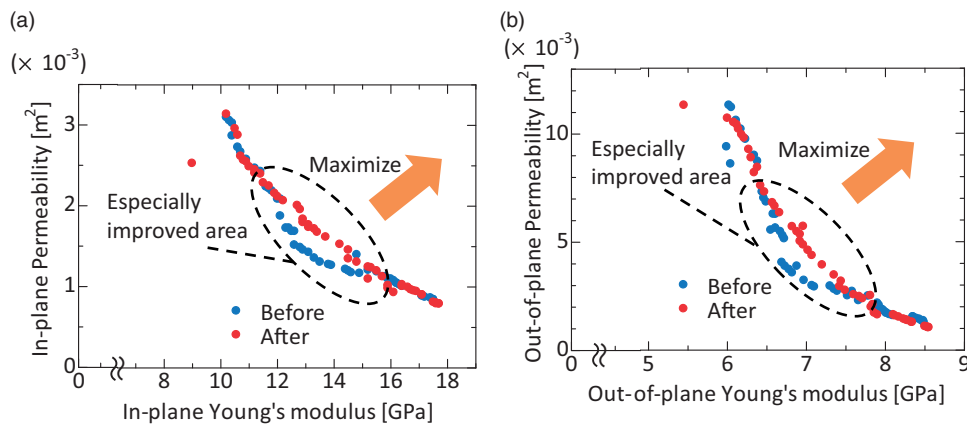


Figure 9. Comparison of the Pareto front of each objective function before and after application of the effective design variables.

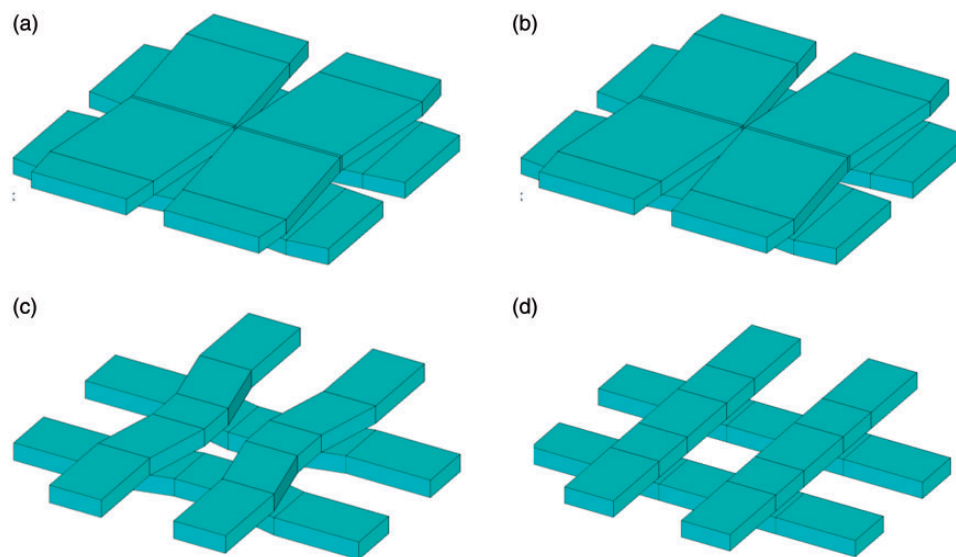


Figure 10. Comparison of the maximum values of each objective function before and after application of the effective design variables. (a) In-plane Young's modulus, (b) Out-of-plane Young's modulus, (c) In-plane permeability and (d) Out-of-plane permeability.

the respective objective functions and the optimal dimensions for each objective function are shown in Table 2. From Figure 10 and Table 2, we observe that the change rate of the fiber-bundle width (x_4) exhibits an interdependent relationship between the elastic modulus and the permeability coefficients; the maximum modulus has maximum x_4 , while the maximum permeability has minimum x_4 . This implies that the fiber-bundle width (x_4) is attributed to the trade-off for the elastic modulus and the permeability coefficients. This is because, as x_4 increases, the transverse fiber bundles spread in the in-plane direction, which increases the elastic modulus. On the other hand, the flow path between the fiber bundles decreases, which results in a low permeability.

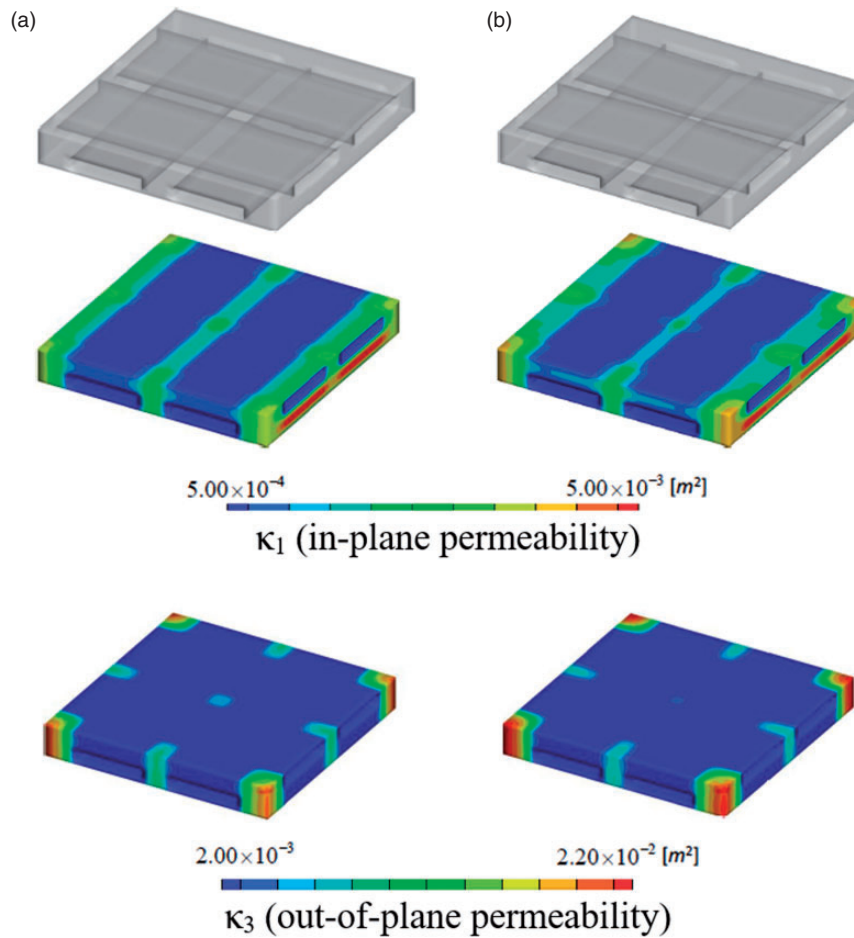
Moreover, by comparing Figure 10(c) and (d), the fiber-bundle offset (x_5) exhibits an interdependent

relationship between the in-plane and out-of-plane permeability coefficients; the maximum in-plane permeability has maximum x_5 , while the maximum out-of-plane permeability has minimum x_5 . This implies that the fiber-bundle offset (x_5) is attributed to the trade-off for in-plane and out-of-plane permeability coefficients. This is because, as x_5 increases, the main (i.e. largest) flow path between the fiber bundles located in the adjacent unit cell increases and the in-plane permeability increases, while the projected flow path in the out-of-plane direction decreases. Therefore, the out-of-plane permeability decreases.

As a detailed investigation of the optimized dimensions of NCF, we employed optimized solutions before and after application of effective design variables as an example in Figure 11. Comparing models (a) and (b) in Figure 11, although model (b) has a 2.5% smaller

Table 2. Design variables and objective functions of Pareto solutions having the maximum value of each objective function (numbers marked with yellow are maximum objective function values).

	Design variables					Objective functions			
	x_1	x_2	x_3	x_4	x_5	$E_1(\text{GPa})$	$E_3(\text{GPa})$	$K_1(\text{m}^2)$	$K_3(\text{m}^2)$
In-plane Young's modulus	0.60	0.10	0.30	1.03	0.03	17.9	8.59	7.70×10^{-4}	1.24×10^{-3}
Out-of-plane Young's modulus	0.60	0.10	0.30	1.03	0.03	17.9	8.59	7.70×10^{-4}	1.24×10^{-3}
In-plane permeability	0.30	0.10	0.30	1.00	0.03	10.2	6.01	3.18×10^{-3}	1.15×10^{-2}
Out-of-plane permeability	0.30	0.10	0.30	1.00	0.00	10.2	6.00	3.07×10^{-3}	1.16×10^{-2}



$$\begin{aligned}
 E_1 &= 17.5 & E_3 &= 8.46 \\
 K_1 &= 8.44 \times 10^{-4} & K_3 &= 1.36 \times 10^{-3} \\
 Vf &= 42.9 & x_1 &= 6.00 \times 10^{-1} \\
 x_2 &= 1.00 \times 10^{-1} & x_3 &= 3.01 \times 10^{-1} \\
 x_4 &= 1.00 & x_5 &= 0.00
 \end{aligned}$$

$$\begin{aligned}
 E_1 &= 17.5 & E_3 &= 8.47 \\
 K_1 &= 8.63 \times 10^{-4} & K_3 &= 1.42 \times 10^{-3} \\
 Vf &= 41.8 & x_1 &= 5.85 \times 10^{-1} \\
 x_2 &= 1.00 \times 10^{-1} & x_3 &= 3.05 \times 10^{-1} \\
 x_4 &= 1.03 & x_5 &= 2.89 \times 10^{-2}
 \end{aligned}$$

Figure 11. In-plane and out-of-plane permeability inside the unit cell of the non-crimp fabric obtained by homogenization method. (a) Before application of the effective design variables and (b) After application of the effective design variables.

Table 3. Correlation coefficient between fiber bundle width and each objective function.

	Fiber-bundle width at the end of unit cell (x_1)	Fiber-bundle width at crimp ($x_1 \times x_4$)
In-plane Young's modulus	0.98	0.98
Out-of-plane Young's modulus	0.98	0.99
In-plane permeability	-0.99	-0.98
Out-of-plane permeability	-0.97	-0.96

fiber-bundle width at the end of unit cell (x_1) and a 1.1% lower fiber volume fraction in the unit cell (V_f), model (b) has a 2.3% and 4.4% higher in-plane and out-of-plane permeability, respectively, while maintaining the elastic modulus. This is because the fiber-bundle width at crimp ($x_1 \times x_4$) has a strong influence on the elastic modulus (Table 3), and it is almost the same value between the two models.

In addition, model (b) has a higher permeability than that of model (a) because it has a 2.5% smaller fiber-bundle width at the end of unit cell (x_1), which adversely affects the permeability (Table 3). Moreover, the smaller x_1 in model (b) means the expansion of the high permeability region. From those facts, by adding the parameter of change rate of the fiber-bundle width ($x_4 > 1$), the fiber-bundle width at the end of unit cell (x_1) can be suppressed while maintaining the fiber-bundle width at the crimp ($x_1 \times x_4$), which enables attainment of the high modulus and permeability.

Conclusions

We proposed an optimization method for the stiffness and permeability of CFRP mesostructures by using a homogenization method. The method generates effective design variables from optimization results derived from a smaller number of design variables. Furthermore, the relationships between the objective functions and design variables are formulated into mathematical expressions that are based on statistical parameters. We examined the effectiveness of the proposed method by considering the optimization problems of the mesostructures of NCF. In this application, we newly derived the effective design variables as the change rate of the fiber-bundle width and fiber-bundle offset in the NCF model in addition to the initial variables. By reflecting the design knowledge, we conducted another optimization.

The results confirmed that the fiber material structure attained higher elastic and permeability coefficients compared to the case where the design knowledge was not applied. In addition, from the investigation of optimization results, we also clarified the trade-off

relationship between the in-plane and out-of-plane elastic modulus and permeability, as well as the effects of dimensions of NCF mesostructures on the elastic modulus and permeability. In this study, we set the in-plane and out-of-plane stiffness and permeability along the axis as objective functions. Consideration of these properties along an arbitrary direction as objective functions may expand the performance space; hence, this will be investigated in future work.

Acknowledgements

The authors acknowledge the vitally important encouragement and support made through the University of Washington-Tohoku University: Academic Open Space (UW-TU:AOS).

Declaration of Conflicting Interests

The author(s) declared no potential conflicts of interest with respect to the research, authorship, and/or publication of this article.

Funding

The author(s) disclosed receipt of the following financial support for the research, authorship, and/or publication of this article: The Cross-ministerial Strategic Innovation Promotion Program (Funding agency: JST, Japan).

ORCID iD

Ryosuke Matsuzaki  <http://orcid.org/0000-0001-8237-1638>
Shigeki Yashiro  <http://orcid.org/0000-0001-5266-2039>

References

1. Kouznetsova VG, Geers MGD and Brekelmans WAM. Multi-scale second-order computational homogenization of multi-phase materials: a nested finite element solution strategy. *Comput Meth Appl Mech Eng* 2004; 193: 5525–5550.
2. Takano N, Zako M, Okazaki T, et al. Microstructure-based evaluation of the influence of woven architecture on permeability by asymptotic homogenization theory. *Compos Sci Technol* 2002; 62: 1347–1356.
3. Song YS and Youn JR. Asymptotic expansion homogenization of permeability tensor for plain woven fabrics. *Compos A Appl Sci Manufact* 2006; 37: 2080–2087.
4. Terada K, Ito T and Kikuchi N. Characterization of the mechanical behaviors of solid-fluid mixture by the homogenization method. *Comput Meth Appl Mech Eng* 1998; 153: 223–257.
5. Bendsoe MP and Kikuchi N. Generating optimal topologies in structural design using a homogenization method. *Comput Meth Appl Mech Eng* 1988; 71: 197–224.
6. Kobayashi M, Nishiwaki S, Izui K, et al. An innovative design method for compliant mechanisms combining structural optimisations and designer creativity. *J Eng Design* 2009; 20: 125–154.
7. Yamada T, Nishiwaki S, Izui K, et al. A structural optimization method incorporating level set boundary

- expressions based on the concept of the phase field method. *J Environ Eng* 2011; 6: 567–578.
8. Wang MY, Wang X and Guo D. A level set method for structural topology optimization. *Comput Meth Appl Mech Eng* 2003; 192: 227–246.
 9. Guest JK and Prévost JH. Optimizing multifunctional materials: design of microstructures for maximized stiffness and fluid permeability. *Int J Solid Struct* 2006; 43: 7028–7047.
 10. Tatsukawa T, Nonomura T, Oyama A, et al. Aerodynamic design exploration for reusable launch vehicle using genetic algorithm with Navier Stokes solver. *Transact Jpn Soc Aeronaut Space Sci Aerosp Technol Jpn* 2012; 10: Pe_55–Pe_63.
 11. Jeong S, Murayama M and Yamamoto K. Efficient optimization design method using Kriging model. *J Aircraft* 2005; 42: 413–420.
 12. Kosugi Y, Oyama A, Fujii K, et al. Multidisciplinary and multi-objective design exploration methodology for conceptual design of a hybrid rocket. In: *Infotech@ Aerospace conferences*, St. Louis, Missouri, US, 2011, AIAA. DOI: 10.2514/6.2011-1634.
 13. Tatsukawa T, Oyama A and Fujii K. Extraction of design information from pareto-optimal solutions using genetic programming: a first report. In: *International workshop on future of CFD and aerospace sciences*, Kobe, Japan, 2012.
 14. Obayashi S, Jeong S and Chiba K. Multi-objective design exploration for aerodynamic configurations. In: *35th AIAA fluid dynamics conference and exhibit, American Institute of Aeronautics and Astronautics*, 2005, AIAA. DOI: 10.2514/6.2005-4666.
 15. Deb K, Agrawal S, Pratap A, et al. A fast elitist non-dominated sorting genetic algorithm for multi-objective optimization: NSGA-II. In: Schoenauer M, et al. (eds) *Parallel Problem Solving from Nature PPSN VI. PPSN 2000. Lecture Notes in Computer Science*. Vol 1917. Berlin, Heidelberg: Springer, 2000, pp.849–858. DOI: 10.1007/3-540-45356-3_83.
 16. Akaike H. A new look at the statistical model identification. *IEEE Transact Automat Control* 1974; 19: 716–723.
 17. Berk KN. Tolerance and condition in regression computations. *J Am Stat Assoc* 1977; 72: 863–866.
 18. Affdl JCH and Kardos JL. The Halpin-Tsai equations: a review. *Polym Eng Sci* 1976; 16: 344–352.
 19. Gebart BR. Permeability of unidirectional reinforcements for RTM. *J Compos Mater* 1992; 26: 1100–1133.
 20. Sanchez-Palencia E. *Non-homogeneous media and vibration theory*. Lecture Notes in Physics, 127. New York: Springer Verlag, 1978.
 21. Mei C. Method of homogenization applied to dispersion in porous media. *Transp Porous Med* 1992; 9: 261–274.
 22. Mei CC, Auriault J-L and Ng C-O. Some applications of the homogenization theory. *Adv Appl Mech* 1996; 32: 277–348.
 23. Ulrich H. *Homogenization and porous media*. New York: Springer-Verlag Inc., 1997.
 24. Nedanov PB and Advani SG. Numerical computation of the fiber preform permeability tensor by the homogenization method. *Polym Compos* 2002; 23: 758–770.
 25. Wang JG, Leung CF and Chow YK. Numerical solutions for flow in porous media. *Int J Numer Anal Meth Geomech* 2003; 27: 565–583.
 26. Sert C. Lecture Notes for ME 582. *Finite element analysis in thermofluids*. In: Cüneyt Sert (ed.) *Incompressible flow solutions*. Department of Mechanical Engineering Middle East Technical University, 2016.
 27. Rogers WH and Wagner TJ. A finite sample distribution-free performance bound for local discrimination rules. *Ann Stat* 1978; 6: 506–514.
 28. Loendersloot R. *The structure-permeability relation of textile reinforcements*. PhD Thesis, University of Twente, Enschede, The Netherlands, 2006. Available at: <https://research.utwente.nl/en/publications/the-structure-permeability-relation-of-textile-reinforcements>.
 29. Franca LP and Frey SL. Stabilized finite element methods: II. The incompressible Navier-Stokes equations. *Comput Meth Appl Mech Eng* 1992; 99: 209–233.
 30. Berdichevsky AL and Cai Z. Preform permeability predictions by self-consistent method and finite element simulation. *Polym Compos* 1993; 14: 132–143.
 31. Verleye B, Klitz M, Crose R, et al. Predicting the permeability of textile reinforcements via a hybrid navier-stokes/brinkman solver. In: *Proceedings of the 8th international conference on flow processes in composite materials (FPCM8)*, Douai, France, 2006.

Appendix I

Calculation process of characteristic function κ_i^j

The detailed calculation process of characteristic function κ_i^j from equations (30) and (31) is described below. First, equation (30) is incorporated into equation (31) to give

$$-\frac{\partial^2 \kappa_i^j}{\partial y_k \partial y_k} - \frac{\partial^2 \kappa_i^j}{\partial y_l \partial y_l} + \frac{\partial A_j}{\partial y_i} = \delta_{ij} \quad (41)$$

Equations (30) and (41) are transformed into the weak form using the Galerkin method.

$$\int_{\Omega} -w_c \frac{\partial \kappa_i^j}{\partial y_i} d\Omega = 0 \quad (42)$$

$$\int_{\Omega} \left[\frac{\partial w}{\partial y_k} \frac{\partial \kappa_i^j}{\partial y_k} + \frac{\partial w}{\partial y_l} \frac{\partial \kappa_i^j}{\partial y_l} - \frac{\partial w}{\partial y_i} A_j \right] d\Omega = \int_{\Omega} w \delta_{ij} d\Omega + \int_{\Gamma} w t_i d\Gamma \quad (43)$$

where t_i is given as follows

$$t_i = \frac{\partial \kappa_i^j}{\partial y_k} n_k + \frac{\partial \kappa_i^j}{\partial y_l} n_l - A_j n_i \quad (44)$$

In equation (43), the area integral term becomes zero because the weighting function is set to be zero on the boundary. Then, the characteristic functions κ_i^j and A_j

are discretized based on FEM as follows

$$\begin{aligned} \kappa_i^j &= \sum_{m=1}^{NEN\kappa} N_m \kappa_{im}^j \\ A_j &= \sum_{m=1}^{NENA} M_m A_{jm} \end{aligned} \quad (45)$$

where κ_{im}^j is a characteristic function of the flow velocity at node; A_{jm} is the characteristic function of the pressure at the node; N_m and M_m represent shape functions; and $NEN\kappa$ and $NENA$ denote the respective numbers of κ_{im}^j and A_{jm} nodes over an element.

It should be noted that the weight function is the same as the shape function as follows

$$\begin{aligned} w &= N_n \\ w_c &= M_n \end{aligned} \quad (46)$$

where n represents the constituent node number of an element. Equations (45) and (46) are substituted into equation (42) to derive

$$\sum_{m=1}^{NEN\kappa} \left[\int_{\Omega} -M_n \frac{\partial N_m}{\partial y_i} d\Omega \right] \kappa_{im}^j = 0 \quad (47)$$

Equations (45) and (46) are substituted into Equation (43) to derive

$$\begin{aligned} \sum_{m=1}^{NEN\kappa} \left[\int_{\Omega} \left(\frac{\partial N_n}{\partial y_k} \frac{\partial N_m}{\partial y_k} \right) d\Omega \right] \kappa_{im}^j + \sum_{m=1}^{NEN\kappa} \left[\int_{\Omega} \left(\frac{\partial N_n}{\partial y_l} \frac{\partial N_m}{\partial y_l} \right) d\Omega \right] \kappa_{lm}^j \\ + \sum_{m=1}^{NENA} \left[\int_{\Omega} -\frac{\partial N_n}{\partial y_i} M_m d\Omega \right] A_{jm} = \int_{\Omega} N_n \delta_{ij} d\Omega \end{aligned} \quad (48)$$

Equation (48) can be expressed as equation (49) in expanded form

$$\begin{aligned} \sum_{m=1}^{NEN\kappa} \left[\int_{\Omega} \left(2 \frac{\partial N_n}{\partial y_1} \frac{\partial N_m}{\partial y_1} + \frac{\partial N_n}{\partial y_2} \frac{\partial N_m}{\partial y_2} + \frac{\partial N_n}{\partial y_3} \frac{\partial N_m}{\partial y_3} \right) d\Omega \right] \kappa_{1m}^1 \\ + \sum_{m=1}^{NEN\kappa} \left[\int_{\Omega} \frac{\partial N_n}{\partial y_2} \frac{\partial N_m}{\partial y_1} d\Omega \right] \kappa_{2m}^1 \\ + \sum_{m=1}^{NEN\kappa} \left[\int_{\Omega} \frac{\partial N_n}{\partial y_3} \frac{\partial N_m}{\partial y_1} d\Omega \right] \kappa_{3m}^1 \\ + \sum_{m=1}^{NENA} \left[\int_{\Omega} -\frac{\partial N_n}{\partial y_1} M_m d\Omega \right] A_{1m} \\ = \int_{\Omega} N_n d\Omega \quad (i=1, j=1) \end{aligned}$$

$$\begin{aligned} \sum_{m=1}^{NEN\kappa} \left[\int_{\Omega} \frac{\partial N_n}{\partial y_1} \frac{\partial N_m}{\partial y_2} d\Omega \right] \kappa_{1m}^1 \\ + \sum_{m=1}^{NEN\kappa} \left[\int_{\Omega} \left(\frac{\partial N_n}{\partial y_1} \frac{\partial N_m}{\partial y_1} + 2 \frac{\partial N_n}{\partial y_2} \frac{\partial N_m}{\partial y_2} + \frac{\partial N_n}{\partial y_3} \frac{\partial N_m}{\partial y_3} \right) d\Omega \right] \kappa_{2m}^1 \\ + \sum_{m=1}^{NEN\kappa} \left[\int_{\Omega} \frac{\partial N_n}{\partial y_3} \frac{\partial N_m}{\partial y_2} d\Omega \right] \kappa_{3m}^1 \\ + \sum_{m=1}^{NENA} \left[\int_{\Omega} -\frac{\partial N_n}{\partial y_2} M_m d\Omega \right] A_{1m} = 0 \quad (i=2, j=1) \\ \vdots \end{aligned} \quad (49)$$

Equations (47) and (49) can be expressed in the matrix form

$$\begin{bmatrix} [K^{11}] & [K^{12}] & [K^{13}] & [K^{14}] \\ [K^{21}] & [K^{22}] & [K^{23}] & [K^{24}] \\ [K^{31}] & [K^{32}] & [K^{33}] & [K^{34}] \\ [K^{41}] & [K^{42}] & [K^{43}] & [K^{44}] \end{bmatrix} \begin{bmatrix} \{\kappa_1^j\} \\ \{\kappa_2^j\} \\ \{\kappa_3^j\} \\ \{A_j\} \end{bmatrix} = \begin{bmatrix} \{F^{1j}\} \\ \{F^{2j}\} \\ \{F^{3j}\} \\ \{F^{4j}\} \end{bmatrix} \quad (50)$$

K^{ij} ($i=1, 2, 3$, and $j=1, 2, 3, 4$) in equation (50) corresponds to the left side of equation (49) and is expressed as

$$\begin{aligned} K_{nm}^{11} &= \int_{\Omega} \left(2 \frac{\partial N_n}{\partial y_1} \frac{\partial N_m}{\partial y_1} + \frac{\partial N_n}{\partial y_2} \frac{\partial N_m}{\partial y_2} + \frac{\partial N_n}{\partial y_3} \frac{\partial N_m}{\partial y_3} \right) d\Omega \\ K_{nm}^{12} &= \int_{\Omega} \frac{\partial N_n}{\partial y_2} \frac{\partial N_m}{\partial y_1} d\Omega \\ K_{nm}^{13} &= \int_{\Omega} \frac{\partial N_n}{\partial y_3} \frac{\partial N_m}{\partial y_1} d\Omega \\ K_{nm}^{14} &= \int_{\Omega} -\frac{\partial N_n}{\partial y_1} M_m d\Omega \\ K_{nm}^{21} &= \int_{\Omega} \frac{\partial N_n}{\partial y_1} \frac{\partial N_m}{\partial y_2} d\Omega = K_{mn}^{12} \\ K_{nm}^{22} &= \int_{\Omega} \left(\frac{\partial N_n}{\partial y_1} \frac{\partial N_m}{\partial y_1} + 2 \frac{\partial N_n}{\partial y_2} \frac{\partial N_m}{\partial y_2} + \frac{\partial N_n}{\partial y_3} \frac{\partial N_m}{\partial y_3} \right) d\Omega \\ K_{nm}^{23} &= \int_{\Omega} \frac{\partial N_n}{\partial y_3} \frac{\partial N_m}{\partial y_2} d\Omega \\ K_{nm}^{24} &= \int_{\Omega} -\frac{\partial N_n}{\partial y_2} M_m d\Omega \\ K_{nm}^{31} &= \int_{\Omega} \frac{\partial N_n}{\partial y_1} \frac{\partial N_m}{\partial y_3} d\Omega = K_{mn}^{13} \\ K_{nm}^{32} &= \int_{\Omega} \frac{\partial N_n}{\partial y_2} \frac{\partial N_m}{\partial y_3} d\Omega = K_{mn}^{23} \\ K_{nm}^{33} &= \int_{\Omega} \left(\frac{\partial N_n}{\partial y_1} \frac{\partial N_m}{\partial y_1} + \frac{\partial N_n}{\partial y_2} \frac{\partial N_m}{\partial y_2} + 2 \frac{\partial N_n}{\partial y_3} \frac{\partial N_m}{\partial y_3} \right) d\Omega \end{aligned}$$

$$K_{nm}^{34} = \int_{\Omega} -\frac{\partial N_n}{\partial y_3} M_m d\Omega \tag{51}$$

K^{ij} ($i=4$ and $j=1, 2, 3, 4$) in equation (50) corresponds to the left side of equation (47) and is expressed as

$$\begin{aligned} K_{nm}^{41} &= \int_{\Omega} -M_n \frac{\partial N_m}{\partial y_1} d\Omega = K_{mn}^{14} \\ K_{nm}^{42} &= \int_{\Omega} -M_n \frac{\partial N_m}{\partial y_2} d\Omega = K_{mn}^{24} \\ K_{nm}^{43} &= \int_{\Omega} -M_n \frac{\partial N_m}{\partial y_3} d\Omega = K_{mn}^{34} \\ K_{nm}^{44} &= 0 \end{aligned} \tag{52}$$

F^{ij} ($i=1, 2, 3$ and $j=1, 2, 3$) in equation (50) corresponds to the right side of equation (49) and is expressed as

$$\begin{aligned} F_n^{1j} &= \int N_n \delta_{1j} d\Omega \\ F_n^{2j} &= \int N_n \delta_{2j} d\Omega \\ F_n^{3j} &= \int N_n \delta_{3j} d\Omega \end{aligned} \tag{53}$$

Because the right side in equation (47) equals zero

$$F_n^4 = 0 \tag{54}$$

$K_{nm}^{44} = 0$ in equation (52) means that the global stiffness matrix has a zero term on the diagonal, which leads to instability in the iterative solver of the linear equation. To avoid this instability, the pressure approximation must be at least one order lower than the velocity approximation. This is known as the inf-sup condition.²⁹ To meet the inf-sup condition, the mixed interpolation function must be used, which results in complex code and a high computational cost. Therefore, we use the GLS method to stabilize equation (50) instead of using the mixed interpolation function.

In GLS, the following stabilization term is added to equations (42) and (43)

$$\int_{\Omega} \tau L(w) \cdot R(\kappa_i^j, A_j) d\Omega \tag{55}$$

where L and R are as follows

$$L(w_i) = -\frac{1}{\rho} \frac{\partial w_c}{\partial y_i} + \frac{\mu}{\rho} \frac{\partial^2 w_i}{\partial y_j \partial y_j} \tag{56}$$

$$R(\kappa_i^j, A_j) = -\frac{1}{\rho} \frac{\partial A_j}{\partial y_i} + \frac{\mu}{\rho} \frac{\partial^2 \kappa_i^j}{\partial y_k \partial y_k} + \delta_{ij} \tag{57}$$

τ is the stabilization parameter and is usually taken to be²⁶

$$\tau = \frac{1}{3} \frac{l_e^2}{4\nu} \tag{58}$$

where l_e is the measure of the element length, and ν is the kinetic viscosity. The stabilization term that is added to equation (42) is

$$\int_{\Omega} \tau \left(\frac{1}{\rho} \frac{\partial w_c}{\partial y_i} \right) \left(-\frac{\mu}{\rho} \frac{\partial^2 \kappa_i^j}{\partial y_l \partial y_l} + \frac{1}{\rho} \frac{\partial A_j}{\partial y_i} - \delta_{ij} \right) d\Omega \tag{59}$$

The stabilization term that is added to equation (43) is

$$\int_{\Omega} \tau \left(-\frac{\mu}{\rho} \frac{\partial^2 w_i}{\partial y_l \partial y_l} \right) \left(-\frac{\mu}{\rho} \frac{\partial^2 \kappa_i^j}{\partial y_m \partial y_m} + \frac{1}{\rho} \frac{\partial A_j}{\partial y_i} - \delta_{ij} \right) d\Omega \tag{60}$$

Here, when the second derivative terms in equations (59) and (60) are assumed to be zero, only equation (59) remains, and it is expressed as

$$\int_{\Omega} \tau \left(\frac{\partial w_c}{\partial y_i} \frac{\partial A_j}{\partial y_i} - \frac{\partial w_c}{\partial y_i} \delta_{ij} \right) d\Omega \tag{61}$$

For simplicity of calculation, ρ is taken to be one. Therefore, $[K^{44}]$ and $\{F^4\}$ in equation (50) are as follows

$$K_{nm}^{44} = \int_{\Omega} -\tau \left(\frac{\partial M_n}{\partial y_k} \frac{\partial M_m}{\partial y_k} \right) d\Omega \tag{62}$$

$$F_n^4 = \int_{\Omega} -\tau M_n \left(\frac{\partial \delta_{ij}}{\partial y_i} \right) d\Omega = 0 \tag{63}$$

Equation (62) indicates that the zero diagonal term of the global system in equation (50) is removed, and the characteristic function κ_i^j can be obtained without the instability problem.

Appendix 2

Validation of homogenized permeability calculation

We validated the homogenized permeability calculation compared with well-known permeability models: Gebart¹⁹ and Berdichevsky.³⁰ Both models used here assume the use of square-arrangement unidirectional

fiber-reinforced material and are expressed as

$$K_{//} = \frac{8R^2(1 - V_f)^3}{57 V_f^2} \quad (65)$$

Gebart model

$$K_{\perp} = \frac{16}{9\pi\sqrt{2}} \left(\sqrt{\frac{\pi}{4V_f}} - 1 \right)^{5/2} R^2 \quad (64)$$

Berdichevsky model

$$K_{\perp} = \frac{R^2}{8V_f} \left(\ln \frac{1}{V_f} - \frac{1 - V_f^2}{1 + V_f^2} \right) \quad (66)$$

$$K_{//} = \frac{R^2}{8V_f} \left(\ln \frac{1}{V_f^2} - (3 - V_f)(1 - V_f) \right) \quad (67)$$

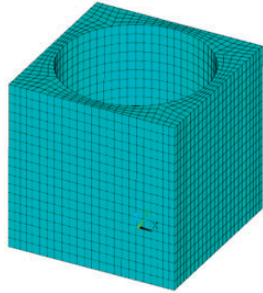


Figure 12. Micro-model of a square arrangement unidirectional fiber-reinforced material used to calculate the homogenized permeability coefficient.

where R is the fiber radius, and K_{\perp} and $K_{//}$ are the permeability in the transverse and parallel flow to the fiber, respectively. The finite models in the case of $V_f=60\%$ are shown in Figure 12. For simplicity, the resin viscosity is set to one.

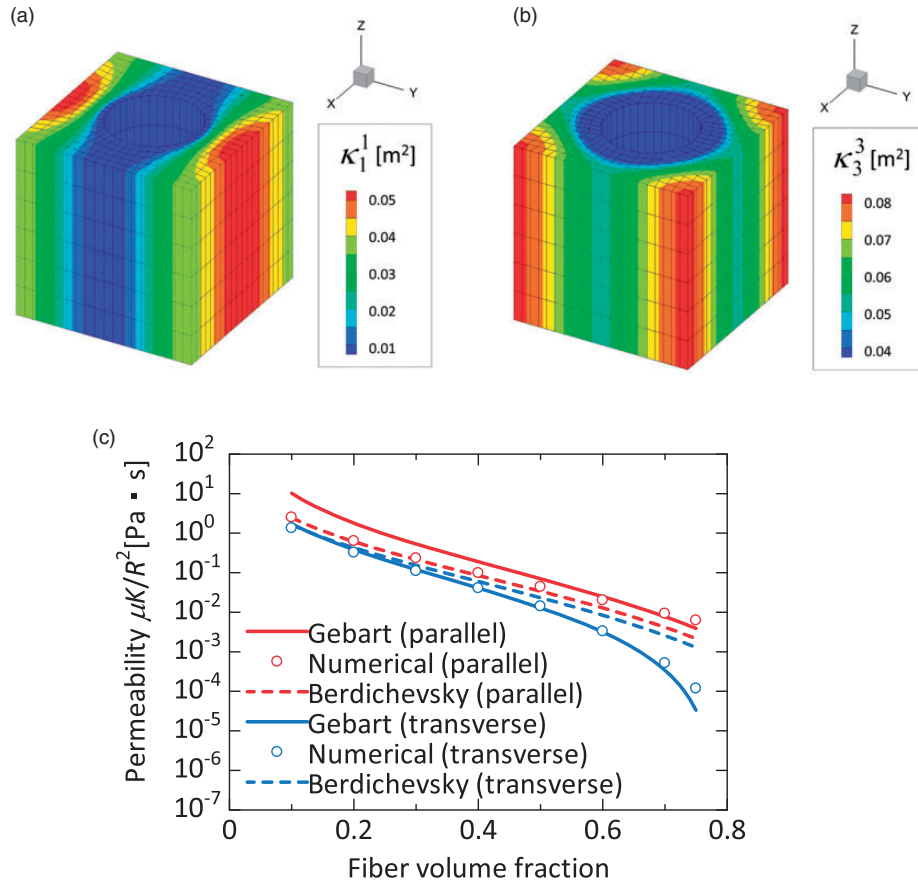


Figure 13. Validation results of homogenized permeability calculation for square arrangement of unidirectional fiber-reinforced material. (a) Characteristic flow-velocity profile in transverse flow to the fiber (κ_1^1) and (b) parallel flow to the fiber (κ_3^3), where the fiber-volume fraction is 20%. (c) Relationship between fiber-volume fraction and permeability obtained from the Gebart model, Berdichevsky model, and homogenization method.

The calculation results of the characteristic flow velocity profile are shown in Figure 13(a) and (b) in the case of $V_f=20\%$. The relationship between the fiber-volume fraction in the unit cell and the calculated homogenized permeability is shown in Figure 13(c). In the transverse flow, the calculation

results agree with the Gebart model. In the parallel flow, the calculation results agree with the Berdichevsky model for low V_f , whereas they agree with the Gebart model for high V_f . This tendency is consistent with that of Verleye et al.³¹